

# Structural and Electrical Properties of Conducting Diamond Nanowires

Kamatchi Jothiramalingam Sankaran,<sup>†</sup> Yen-Fu Lin,<sup>‡</sup> Wen-Bin Jian,<sup>‡</sup> Huang-Chin Chen,<sup>§</sup> Kalpataru Panda,<sup>⊥</sup> Balakrishnan Sundaravel,<sup>⊥</sup> Chung-Li Dong,<sup>#</sup> Nyan-Hwa Tai,<sup>\*,†</sup> and I-Nan Lin<sup>\*,§</sup>

<sup>†</sup>Department of Materials Science and Engineering, National Tsing Hua University, Hsinchu 30013, Taiwan, ROC

<sup>‡</sup>Department of Electrophysics, National Chiao Tung University, Hsinchu 30010, Taiwan, ROC

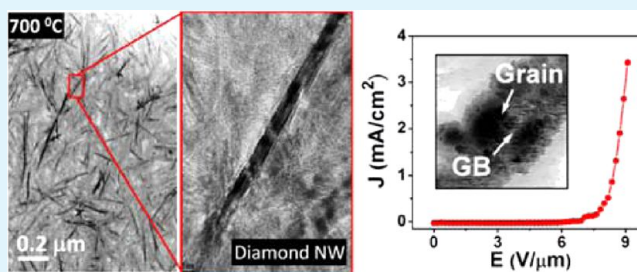
<sup>§</sup>Department of Physics, Tamkang University, Tamsui 251, Taiwan, ROC

<sup>⊥</sup>Materials Science Group, Indira Gandhi Centre for Atomic Research, Kalpakkam 603 102, India

<sup>#</sup>Scientific Research Division, National Synchrotron Radiation Research Center, Hsinchu 30076, Taiwan, ROC

**ABSTRACT:** Conducting diamond nanowires (DNWs) films have been synthesized by N<sub>2</sub>-based microwave plasma enhanced chemical vapor deposition. The incorporation of nitrogen into DNWs films is examined by C 1s X-ray photoemission spectroscopy and morphology of DNWs is discerned using field-emission scanning electron microscopy and transmission electron microscopy (TEM). The electron diffraction pattern, the visible-Raman spectroscopy, and the near-edge X-ray absorption fine structure spectroscopy display the coexistence of sp<sup>3</sup> diamond and sp<sup>2</sup> graphitic phases in DNWs films. In addition, the microstructure investigation, carried out by high-resolution TEM with Fourier transformed pattern, indicates diamond grains and graphitic grain boundaries on surface of DNWs. The same result is confirmed by scanning tunneling microscopy and scanning tunneling spectroscopy (STS). Furthermore, the STS spectra of current–voltage curves discover a high tunneling current at the position near the graphitic grain boundaries. These highly conducting regimes of grain boundaries form effective electron paths and its transport mechanism is explained by the three-dimensional (3D) Mott's variable range hopping in a wide temperature from 300 to 20 K. Interestingly, this specific feature of high conducting grain boundaries of DNWs demonstrates a high efficiency in field emission and pave a way to the next generation of high-definition flat panel displays or plasma devices.

**KEYWORDS:** diamond nanowire films, graphitic grain boundary, high resolution transmission electron microscopy, scanning tunneling spectroscopy, hopping transport, electron field emission



## 1. INTRODUCTION

Field-emission displays (FEDs) have received interest as the next-generation flat panel displays, substitute to the presently dominant liquid crystal, because of their potential low cost and high performance. One of the major concerns in FEDs has been the improvement of consistent, efficient cold cathode materials for electron field emitters.<sup>1–4</sup> Materials like semiconductor nanowires or nanotubes, carbon nanotubes (CNTs), and diamond films have been demonstrated to show low turn-on voltages and high current densities, making them suitable for cold cathode emitter applications. Among them, diamond films have been reported to exhibit negative electron affinity, which makes diamond a more promising material for applications in FED devices.<sup>5–8</sup> On the other hand, one-dimensional (1D) materials showing distinct chemical and physical properties have attracted a tremendous amount of attention and have been used in many technological applications such as pH sensors,<sup>9</sup> ultraviolet nanolasers,<sup>10</sup> and nanoelectronics.<sup>11–13</sup> Since the discovery of CNTs in 1991,<sup>14</sup> a variety of 1D materials were successfully synthesized.<sup>10,15</sup> Among those 1D materials,

diamond nanowires (DNWs) were of great interest because theoretical studies and simulations explain their structural stabilities and inspire several potential applications.<sup>16–18</sup> Especially, through their intrinsic dependence on size and crystallographic directions, DNWs were found to be energetically favored and structurally stable at diameters ranging from 2.7 to 9.0 nm.<sup>16,17</sup> Recently, novel properties including high thermal conductivity and zero strain stiffness of DNWs and related carbon materials have been theoretically predicted and experimentally demonstrated, foreseeing their feasible use in cross-link facilitated heat transfer and thermal management systems.<sup>19,20</sup>

The synthesis of DNWs is always an interesting subject since new approaches pave the way to nanoscale and atomic precision of material growth and to the search of new forms of carbon. The DNW precursor of porous diamond films was

Received: October 22, 2012

Accepted: January 17, 2013

Published: January 17, 2013

successfully fabricated by reactive ion etching in  $O_2$  and  $CF_4$  plasma.<sup>21</sup> Thereafter, nanostructured diamond honeycomb films were prepared by oxygen plasma etching with porous anodic alumina mask.<sup>22</sup> Very recently, DNWs of 80–100 nm in length were synthesized in ultrananocrystalline diamond (UNCD) films which was deposited by microwave plasma-enhanced chemical-vapor deposition (MPECVD) system with an introduction of nitrogen in the mixture gas.<sup>23,24</sup> Generally, UNCD films prepared in  $Ar/CH_4$  microwave plasma were electrically insulating<sup>25</sup> and amorphous carbon (a-C) phases contained in the grain boundaries of UNCD films is not sufficiently high and therefore limits the electron field-emission (EFE) properties attainable for UNCD films.<sup>26</sup> Incorporation of  $N_2$  (about 20%) in  $Ar/CH_4$  plasma generated a nanowire morphology and rendered the UNCD films a high electrical conductivity. Through microscopy and other physical inspections, it was further argued that the notable increase in conductivity was in relation to the fact of nanowires encased by a sheath of  $sp^2$ -bonded carbon.<sup>23,27–29</sup> Additionally, the incorporation of  $N_2$  was preferentially in the diamond grain boundary<sup>30</sup> that enhances the electron transport in UNCD films and demonstrates a prominent potential for an application as an electron field emitter.<sup>26,31</sup> Nevertheless, the mechanisms of a high conductivity in DNWs and their superior EFE behavior are not well understood yet.

To solve the issue of conducting mechanism in DNWs, the temperature behavior of resistivity that unveils the electron transport in DNWs need to be explored in detail. In a previous report, temperature-dependent resistivity of  $N_2$ -doped UNCD films was obtained and thermally activated conduction mechanisms with different activation energies were noticed.<sup>27</sup> Besides, it was proposed that the enhanced conductivity exists in diamond grain boundaries. Moreover, latter studies show that Mott's three-dimensional variable range hopping (3D VRH) theory, Efros-Shklovskii's hopping conduction, or other new integrated model of hopping conduction were adopted to analyze data of lightly or heavily  $N_2$ -doped UNCD films.<sup>32–34</sup> The heavily doped UNCD films were like a special kind of disordered metal, showing a negative magnetoresistance of weak localization<sup>35</sup> or a logarithmic temperature-dependent conductivity of electron–electron interaction.<sup>36</sup> However, it was theoretically argued that the negative magnetoresistance originates from strong rather than weak localization.<sup>37</sup> On the other hand, in the temperature range from 300 to 700 K the high conductivity of UNCD films can be explained by a transition from Mott's 3D VRH to defect-band conduction transport.<sup>38</sup> Until now, the conduction mechanism in DNWs has not been studied from both microscopically and macroscopically electrical measurements.

In this paper, we reported the electrical mechanism of the enhanced conductivity and EFE characteristics of DNWs films from a microscopic viewpoint by using scanning tunneling microscope (STM) and scanning tunneling spectroscopy (STS). The conducting regimes at both grains and grain boundaries were examined in detail. Moreover, the microscopic picture of conducting mechanism can be integrated with a macroscopic (or mesoscopic) viewpoint of electron transport obtained from the temperature dependent resistivity with a careful analysis.

## 2. EXPERIMENTAL SECTION

**2.1. Growth of DNWs Films.** DNWs films with a thickness of  $\sim 800$  nm were grown on mirror polished Si (100) substrates by using

MPECVD system (2.45 GHz 6 in. IPLAS-CYRANNUS). Prior to deposition, the substrates were ultrasonicated in methanol solution containing nanodiamond ( $\sim 5$  nm in diameter) powders and titanium ( $\sim 325$  mesh) powders for 30 min to facilitate nucleation of DNWs. DNWs films were deposited on the preseeded substrates by MPECVD in a  $N_2$  (94%)/ $CH_4$  (6%) plasma with a microwave power of 1200 W. The pressure and the flow rate were maintained at 50 Torr and 100 sccm, respectively. The substrate temperature that was monitored by a thermocouple was heated at a temperature of 700 °C.

**2.2. Material Characterizations.** The morphology and microstructure of the as-deposited DNWs films were examined using field-emission scanning electron microscope (FESEM; JEOL-6500) and transmission electron microscope (TEM; JEOL-2100 operated at 200 kV). In addition, the films were further characterized by visible-Raman spectroscopy (Lab Raman HR800, Jobin Yvon,  $\lambda$ : 632.8 nm), X-ray photoemission spectroscopy (XPS; PHI 1600), secondary ion mass spectroscopy (SIMS; Cameca IMS-4f) and near-edge X-ray absorption fine structure (NEXAFS) spectroscopy. Hall measurements were carried out in a van der Pauw configuration (ECOPIA HMS-3000) to measure the electrical conductivity of the films.

**2.3. Electrical Measurements.** Conducting paths in DNWs films at either grains or grain boundaries were investigated elaborately by STM (150 Aarhus, SPECS GmbH) in an ultrahigh vacuum of  $10^{-10}$  Torr at room temperature (RT). STM tips were prepared by electrochemical etching of tungsten wires with a diameter of 0.3 mm. STM images were taken in a constant current mode with a set current of 0.59 nA and a bias voltage of  $-3.75$  V. Current image tunneling spectra (CITS) with voltages ramping from  $-5$  to 5 V were measured simultaneously during the STM image scanning. A STS spectrum was calculated from an average of many CITS data.

To address electron transport mechanism of the DNWs films from macroscopic viewpoint, the DNWs films were put on a prepatterned device substrate with pairing electrodes separated by a  $\sim 200$ -nm wide gap for temperature dependence of electrical measurements. Si wafers capped with a 300-nm  $SiO_2$  layer were used as device substrates for deposition of patterned, pairing Ti/Au (10/50 nm in thickness) electrodes. By etching in  $HF:HNO_3$  (1:1) solution, DNWs films were detached from growth substrates and formed free-standing films in the solution. The free-standing DNWs films were dispersed in acetone. A prepatterned device substrate containing pairing electrodes was then immersed into this solution and was moved up slowly such that the DNWs deposited onto the device randomly when the acetone dried. No special effort was needed to immobilize the DNWs. The DNWs films were checked to make an Ohmic contact on top of Ti/Au electrodes.<sup>39</sup> The pairing electrodes were taken as source and drain electrodes for probing electrical properties of DNWs sitting in  $\sim 200$  nm wide nanogap. The as-fabricated DNWs devices were mounted in a closed-cycle refrigerator (CRYO Industries of America Inc.) with a background pressure of  $1 \times 10^{-6}$  Torr for temperature dependent studies. Current–voltage ( $I$ – $V$ ) data were measured by Keithley 6430 source meter. Electrical conductance was calculated in the linear  $I$ – $V$  regime near zero-bias voltage. Conductivities were evaluated from the conductance and the dimensions of DNWs between pairing electrodes.

On the other hand, EFE characteristics of the DNWs were measured using a molybdenum rod with a diameter of 2 mm as anode and  $I$ – $V$  curves were acquired using Keithley 237 electrometer. The EFE behavior of materials was explained using Fowler-Nordheim (F–N) theory.<sup>40</sup> The turn-on field was estimated from the interception of the straight lines extrapolated from the low- and high-field segments of the F–N (viz.  $\ln(J/E^2) - 1/E$ ) plots.

## 3. RESULTS AND DISCUSSION

**3.1. Material Characterizations.** Figure 1a shows a typical low-magnification TEM image of DNWs films, revealing highly dense and uniformly distributed nanowire morphology. These randomly oriented DNWs have a length of 50–200 nm with a few nanometers in diameter. Its FESEM image which reveals the last-minute growth of surface structure is displayed in the

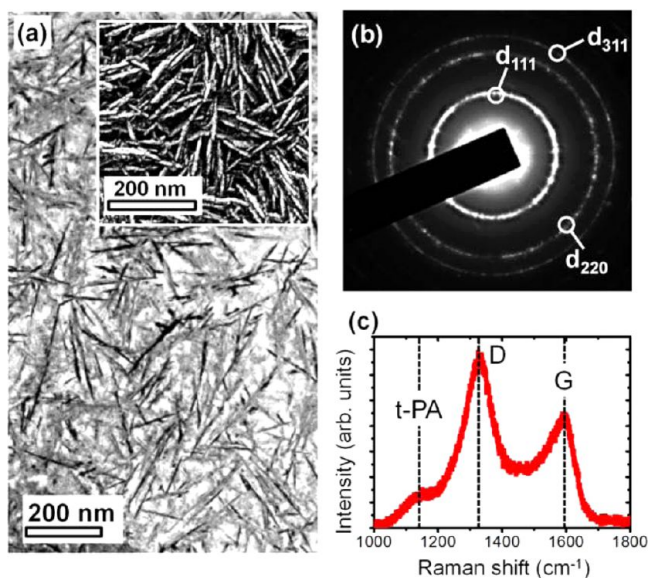


**Figure 1.** (a) Low-magnification TEM image of DNW films. The inset shows FESEM image for comparison. (b) TEM-corresponding SAED pattern, where different lattice-plane spacings of diamond are indicated. (c) visible-Raman spectrum of DNWs films. The characteristic peaks of *trans*-polyacetylene, diamond, and graphite bands are marked as *t*-PA, D, and G, respectively.

inset of Figure 1a. The TEM-corresponding selective area electron diffraction (SAED) pattern of the DNWs film is shown in Figure 1b, which exhibits ring-shaped patterns, implying random orientation of DNWs that are observed in the TEM image (Figure 1a). According to the SAED pattern, the lattice-plane spacings of (311), (220), and (111) are estimated to be 0.11, 0.12, and 0.21 nm, respectively, which are in line with the crystalline diamond structure. The result confirms that DNWs films are mainly constituted of diamond nanocrystals with nanowire morphology. On the other hand, there is a prominent diffusing ring in the center of the SAED pattern, signifying the existence of graphitic phase (or a-C) in DNWs films.

Figure 1c shows a visible-Raman spectrum having an excitation wavelength of 632.8 nm. The spectrum of DNWs shows a predominance of the  $sp^2$ -bonded carbon phase (D-band<sup>41</sup> around  $1335\text{ cm}^{-1}$  and G-band around  $1590\text{ cm}^{-1}$ ). Additionally, a peak at  $1140\text{ cm}^{-1}$  is observed. It corresponds to the *trans*-polyacetylene (*t*-PA) and marks an alternate chain of  $sp^2$  carbon atoms with single hydrogen bonded to each carbon atom.<sup>42–44</sup> Notably, the characteristic diamond resonance peak at  $1332\text{ cm}^{-1}$  is not clearly observable, due to the overwhelmingly high sensitivity of visible-Raman to the  $sp^2$ -bonded structure over that of the  $sp^3$ -bonded one. All these features in both of the visible-Raman scattering and the TEM SAED indicate that the overall structure of DNWs is dominated by the  $sp^2$ -sites in the presence of  $sp^3$ -bonded carbon as well as *t*-PA chains.

Figure 2 shows a NEXAFS C-K edge of DNWs. Except for a typical  $sp^2$ -bonded carbon characteristic peak at 285.0 eV, NEXAFS of DNWs is very similar to that of a single crystalline diamond. It demonstrates unambiguously one specific feature of a diamond exciton sharp peak at 289.0 eV and the other specific feature of a large dip at 302.5 eV which represents a second absolute gap in the diamond band structure.<sup>28,45,46</sup> This corroborates again the coexistence of  $sp^3$  diamond and  $sp^2$  graphitic phases in DNWs films that is in line with the visible-

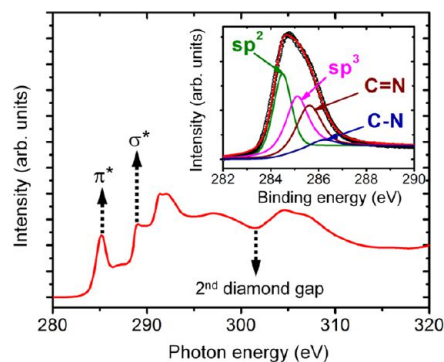


**Figure 2.** NEXAFS C-K edge spectrum of DNWs films. The inset shows C 1s XPS spectrum with four fitting curves to identify carbon binding states.

Raman and TEM results. To understand how nitrogen doping results in the chemical bonding of DNWs more precisely, XPS measurements were carried out. The C 1s photoemission spectrum of DNWs is shown in the inset of Figure 2. The data are fitted with Lorentzian functions to identify peaks at binding energies of 284.5, 285.1, 285.6, and 286.2 corresponding to C=C;  $sp^2$ , C-C;  $sp^3$ , C=N, and C-N bonds, respectively. The background was subtracted using Shirley's method.<sup>47</sup> The  $sp^2$  C=C bonding is predominant with a peak intensity of 35% and  $sp^3$  C-C intensity is 34%. The presence of C=N (26%) and C-N (5%) signifies the existence of nitrogen in the sample. The depth profile in SIMS spectra (figure not shown) also reveals the presence of nitrogen species uniformly along the thickness of DNW films, but the intensity is too low to be counted, and it cannot be differentiated whether the nitrogen species are locating in diamond grains or along the grain boundaries.

To unravel the structure of the DNW, we have completed high-resolution TEM (HRTEM) studies. Figure 3a displays an HRTEM image of a DNW, exhibiting a clear core-shell microstructure. Each DNW is found to be encased by the graphite phase, which probably forms during the growth of DNWs. The thickness of the graphitic layer varies from a few atomic layers to more than 5 nm. To analyze the two crystalline carbon phases of diamond and graphite structures in detail, another HRTEM image (Figure 3b) is taken and its corresponding Fourier transformed (FT) pattern is displayed in the inset. Moreover, the yellow and green spots on the FT diffraction pattern are inversely transformed to address the diamond (area in yellow) and graphite (area in green) phases on the HRTEM image (see Figure 3c). Such a colored HRTEM image in Figure 3c clearly indicates again that the graphitic layer (green region) encases the surface of the DNWs (yellow region). In addition to the graphitic sheath, there are a few nanometer-sized diamond grains randomly oriented near the DNW (marked as X in Figure 3c). The diamond and graphitic structures are further analyzed by FT on selected areas. Figure 3d<sub>1</sub> shows the FT pattern on d<sub>1</sub> area (marked in Figure 3b) giving the ordering of the (111) planes of the diamond structure whereas Figure 3d<sub>2</sub> shows the FT pattern on d<sub>2</sub> area pointing to the ordering of the (111) planes of the graphitic structure. High-magnification HRTEM image of the d<sub>1</sub> area is offered in Figure 3e, which reflects considerably the crystalline nature with a lattice spacing of 0.21 nm. These results confirm that the DNW is encapsulated by a sheath of graphitic phase. The microstructural studies of DNW films



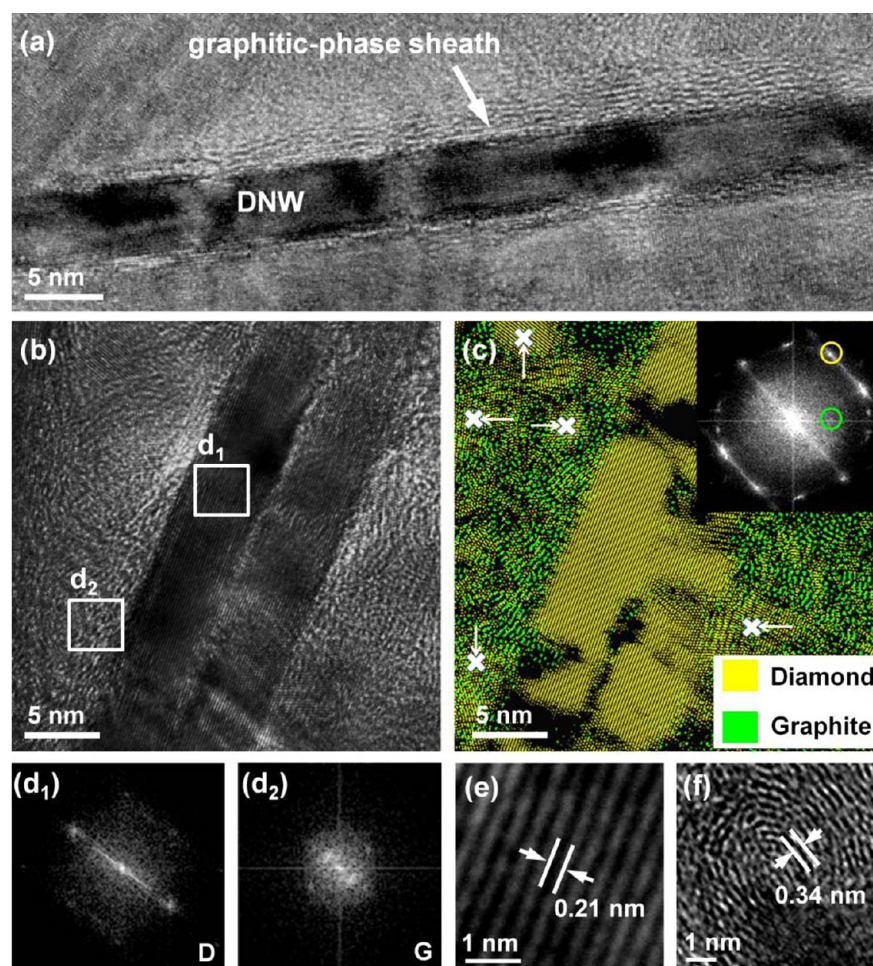


**Figure 3.** (a) HRTEM image of a single DNW disclosing the core–shell microstructure. (b) HRTEM image with its corresponding FT pattern displayed in the inset. (c) Inverse FT image from the inset of b to mark the diamond and graphite regimes. FT patterns of  $d_1$  and  $d_2$  areas in TEM image b are shown in figures  $d_1$  and  $d_2$ , respectively. (e) Crystalline structure of the  $d_1$  area in b presenting a clear (111) planes of the diamond structure with a lattice spacing of 0.21 nm.

confirmed that this graphitic content is formed during the growth of films. The presence of abundant CN species in the N<sub>2</sub>/CH<sub>4</sub> plasma, which was observable in optical emission spectra (figure not shown), may preferentially induce the formation of nanorod, along with the graphitic phase encasing the nanorods.<sup>48,49</sup>

**3.2. Electrical Properties.** Hall measurements in van der Pauw configuration were taken on DNWs films at the millimeter scale at RT so as to measure their electrical conductivities. The negative value of the Hall coefficients indicates that the majority of carriers are electrons in DNWs films. The carrier concentrations, electrical conductivity and mobility of the DNWs films are evaluated to be about  $1.0 \times 10^{20} \text{ cm}^{-3}$ ,  $186 \text{ S cm}^{-1}$ , and  $11.6 \text{ cm}^2/\text{V s}$ . To scrutinize the main conducting paths for electrons from the microscopic viewpoint, CITS and STS spectra measurements were performed to obtain tunneling  $I$ – $V$  curves on DNWs films. Figure 4a shows a typical STM image of a DNW with a length of about 200 nm. The dark area representing a valley place between DNWs is marked as DNWs interval which is the space between DNWs and is about several tens to hundreds of nanometer away from DNWs. Figure 4b presents a CITS image at a sample bias voltage of  $-3.75 \text{ V}$  that corresponds to the STM image in Figure 4a. The bright and high-current region is

close to the DNWs whereas the dark and low-current region is close to the DNWs interval. Additionally, STS spectra of tunneling  $I$ – $V$  curves at the marked position in images a and b in Figure 4 are offered in Figure 4c. The position at the DNWs interval reveals a lower current of an insulating feature while the position on DNWs exposes much higher current to indicate the effective conducting path. The feature can be observed, for example, at a given bias voltage of about 1.4 V the current difference is larger than 2 orders of magnitude. Consequently, the conducting paths are on surface of the DNWs rather than in the interval between DNWs.

The conducting paths on the surface of DNWs are inspected carefully. The zoom-in, high-resolution STM image of the surface of a single DNW is shown in Figure 4d. To examine the microstructure on the surface of the DNW, the STM image in a highly contrast mode is presented in Figure 4e for an easy identification of diamond grains and graphitic grain boundaries. The DNW is made of smaller diamond clusters of equiaxed geometry. The cluster size varies between 2.0 and 5.0 nm which is consistent with that of the diamond grains, incorporated in the conventional UNCD films grown by Ar/CH<sub>4</sub> plasma. Apparently, the grains in the STM image (Figure 4e) are diamond grains which are adhered to get elongation of DNWs (see Figure 3c for the similar feature). In addition, Figure 4f

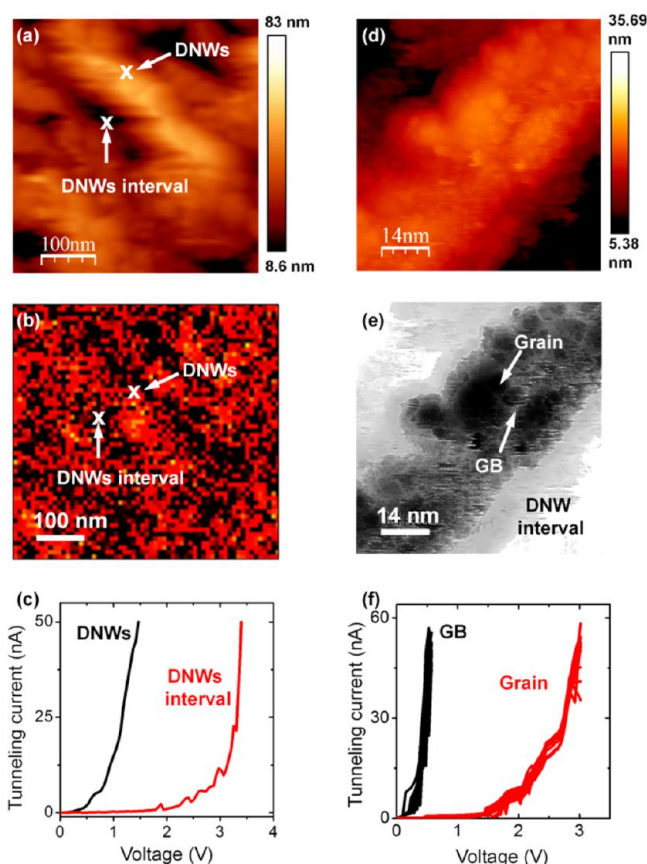


**Figure 4.** (a) STM image DNWs films with (b) its corresponding current image at  $-3.75$  V. The positions of the DNWs and the DNWs interval are marked. (c) The STS spectra (tunneling  $I$ - $V$  curves) at the marked position in a and b. (d) Its high contrast image, to discern diamond grains and grain boundaries on DNWs. (e) High contrast image, to discern diamond grains and grain boundaries on DNWs. (f) STS spectra of tunneling  $I$ - $V$  curves at the marked position in e.

presents the STS spectra of tunneling  $I$ - $V$  curves at the diamond grain (Grain) and graphitic grain boundary (GB) which are marked in Figure 4e. Very excitingly, the tunneling current at the graphitic GB position is much larger than that at the diamond Grain position. From such a microscopic inspection, this result confirms again that the electron conducting path is along the graphitic GB rather than the diamond Grain on the surface of DNWs. It is noted that the average of the two  $-V$  curves in Figure 4f is very close to the  $I$ - $V$  curve (marked as DNWs) manifested in Figure 4c, corroborating the rationalization of the CITS measurements. Moreover, the GB regimes surrounding the isolated Grains assist to establish conducting channels covering on the whole surface of DNWs. The size of GBs is roughly equal to the Grain size of  $\sim 3$  nm. These DNWs are randomly distributed and electrically contacted in the film to form 3D conducting channels; likewise the tunneling  $I$ - $V$  curve at GB demonstrates a very low threshold voltage lower than 0.5 V and a tunneling current higher than 50 nA. Such a special property at GB on surface of DNWs may give superior EFE properties.

On the other hand, DNWs devices were fabricated to probe their electron transport at the hundred-nanometer scale.  $I$ - $V$  characteristics of the DNWs device (DNW1) were obtained (Figure 5a) by sweeping currents and acquiring voltages at various temperatures. At a given voltage, the current of the

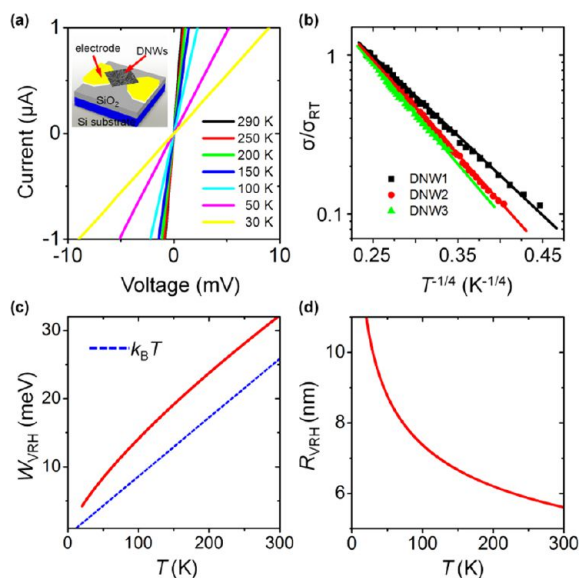


**Figure 5.** (a)  $I$ - $V$  curves of the DNWs device (DNW1) at various temperatures. A schematic diagram of the DNWs device is drawn in the inset. (b) Temperature-dependent conductivities of three different DNWs devices (DNW1-3). The solid lines present the best fits to our data. The conductivities are normalized by dividing with its RT value for comparison with ease. (c) Hopping energy,  $W_{\text{VRH}}$ , as a function of temperature (red curve). The dashed line portrays the thermal energy for comparison. (d) Hopping distance,  $R_{\text{VRH}}$ , as a function of temperature.

DNW1 device increases with a decrease of temperature.  $I$ - $V$  curves are linear up to a large current of  $\pm 1 \mu\text{A}$ , indicating an Ohmic contact between the DNWs film and the Ti/Au electrode. The Ohmic contact ensures the measurement of intrinsic conductivities or resistivity of DNWs. The RT conductivity of the DNW1 device is estimated to be about  $175 \text{ S cm}^{-1}$  which is in excellent line with that obtained by the Hall measurement. A schematic diagram of the DNWs device is depicted in the inset of Figure 5a. It is noted that the separation distance between the pairing electrodes was kept a constant for all devices. Temperature dependent behaviors of three DNWs devices (DNW1-3) are displayed in Figure 5b. The conductivity decreases with decreasing temperature which implies either a thermal activation of semiconductor or a strong localization of a disordered system. In a strong disorder system such as the graphitic phase randomly oriented in grain boundaries and encasing DNWs, electrons are localized in the fluctuated random potential. Therefore, temperature dependent conductivity can be described by the Mott's variable range hopping (VRH) model in accordance with the expression of  $\sigma = \sigma_0 \exp(-T_0/T)^{-1/p}$ ,<sup>50</sup> where  $\sigma$  and  $T$  are conductivity and temperature,  $\sigma_0$  is a weak temperature-dependent constant, and  $T_0$  is a constant of a characteristic temperature. The exponent  $p$  is 2, 3, or 4 for a one-, two-, or three-dimensional (3D) disordered system, respectively. Figure 5b presents the normalized conductivity of the DNWs devices in a logarithm scale showing a linear dependence on  $T^{-1/4}$  at temperature ranges from 300 to 20 K and complying with the Mott's 3D VRH model. The experimental average values of  $\sigma_0$  and  $T_0$  derived from the best fits to data in Figure 5b are about  $20 \text{ S cm}^{-1}$  and  $1.9 \times 10^5 \text{ K}$ , respectively.

To verify the correctness of using the Mott's 3D VRH model, we analyzed the parameters derived from the fits to our data as



follows. The first supporting point is that the derived hopping energy needs to be larger than the thermal energy at that temperature. The hopping energy is defined as  $W_{\text{VRH}} = (1/4) k_{\text{B}}(T_0/T)^{1/4}$ ,<sup>50</sup> where  $k_{\text{B}}$  is Boltzmann constant. Using  $T_0$  of  $1.9 \times 10^5$  K, we estimate the hopping energy to be 32 meV which is larger than the thermal energy of 26 meV at RT. Moreover, the hopping energy at all other temperatures lower than 300 K is lower than its corresponding thermal energy (Figure 5c) which satisfies the criterion of using the Mott's 3D VRH model. The second supporting point is that the hopping distance needs to be longer than the size of the grain boundary of DNWs. The hopping distance is computed by using the equation of  $R_{\text{VRH}} = (3/8)\xi(T_0/T)^{1/4}$ ,<sup>50</sup> where  $\xi$  is the localization length of electrons in DNWs films. Assuming that  $\xi$  as the size of grain boundary on surface of DNWs (about 3 nm), the hopping distance can be estimated to be in the range between 5.6 and 11 nm from 300 to 20 K (Figure 5d). Finally, the last supporting point is that the carrier density evaluated from the  $T_0$  parameter shall be in line with our previous estimation of high conductivity and carrier concentration. The characteristic temperature,  $T_0$ , is described by the form  $T_0 = 18/(k_{\text{B}}g_0\xi^3)$ ,<sup>50</sup> where  $g_0$  is the density of states at Fermi level. Thus we can evaluate  $g_0$  to be about  $2.0 \times 10^{20} \text{ eV}^{-1} \text{ cm}^{-3}$ . Such a high density of states self-consistently supports our previous evaluation of a high carrier concentration as well as a high conductivity of the DNWs film.

**3.3. Application: Electron Field Emission Source.** The EFE properties of the DNWs encased by the highly conducting graphite were tested in order to demonstrate their specific applications in future electronics. Figure 6 presents emission

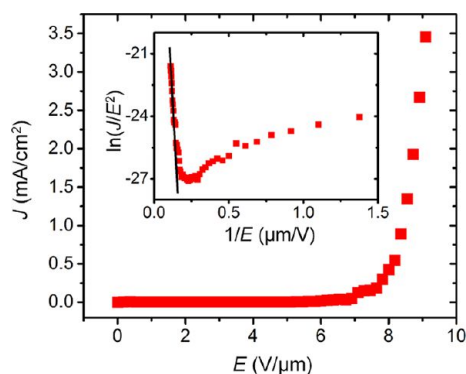


**Figure 6.** Emission current density as a function of applied electric field for DNWs films. The data in the form of  $\ln(J/E^2) - 1/E$  plot are presented in the inset. The solid line indicates a high-field approach fitting by the F–N theory.

current density,  $J$ , as a function of the applied electric field,  $E$ . It reveals a low turn-on field of  $\sim 4.35 \text{ V}/\mu\text{m}$  at a current density of  $3 \mu\text{A}/\text{cm}^2$ . In addition, the current density increases rapidly and reaches the large magnitude of  $\sim 3.42 \text{ mA}/\text{cm}^2$  at the field of  $9.1 \text{ V}/\mu\text{m}$ . In addition, the relationships among the current density ( $J$ ), electric field ( $E$ ), work function ( $\phi$ ) and field enhancement factor ( $\beta$ ) of an emitter are expressed by the F–N equation:  $J = (A\beta^2 E^2 / \phi) \exp(-B\phi^{3/2} / \beta E)$ , where  $A = 1.54 \times 10^{-6} \text{ A eV V}^{-2}$  and  $B = 6.83 \times 10^9 \text{ eV}^{-3/2} \text{ V m}^{-1}$ . We fit the high field segments of the F–N curve to the above equation and the results of the fitting are shown as solid line in the inset of Figure 6, illustrating that the EFE data fit the F–N model very well. We assume that the  $\phi$  value of diamond is assumed as  $5.0 \text{ eV}$ <sup>51</sup> for estimating the  $\beta$  value of DNWs, which is  $\beta = 1024$

from the F–N slope. The DNWs film exhibits far more efficient EFE properties of lowest  $E_0$  and highest  $J_e$  values than that of other diamond related materials reported previously<sup>52–58</sup> and comparable to the carbon-based materials,<sup>59–63</sup> which are summarized in Table 1. This excellent EFE feature of DNWs films evidence a high potential for flat panel display applications.<sup>64</sup>

**Table 1. Comparison on Electron Field Emission Properties of DNW Films with Various Kinds of Carbon Nanostructures**

materials	turn-on field (V/ $\mu\text{m}$ )	current density	field enhancement factor
undoped nanostructured diamond <sup>52</sup>	4.9	10 mA/cm <sup>2</sup>	
boron doped diamond-clad si tips <sup>53</sup>	15.5	90 $\mu\text{A}/\text{cm}^2$	
diamond–nondiamond composite films <sup>54</sup>	9.0	1.9 mA/cm <sup>2</sup>	
Freestanding n-type conducting UNCD films <sup>55</sup>	10	0.20 mA/cm <sup>2</sup>	
c-diamond and n-diamond grains on Si nanoneedles <sup>56</sup>	2.2	2.2 mA/cm <sup>2</sup>	1491
vertically aligned conducting UNCD nanorods <sup>57</sup>	2.04	4.84 mA/cm <sup>2</sup>	1945
free-standing graphene–diamond hybrid films <sup>58</sup>	2.4	0.1 mA/cm <sup>2</sup>	
CNT–graphene hybrid materials <sup>59</sup>	2.9	1.33 mA/cm <sup>2</sup>	1373
open-ended tubular graphite cones <sup>60</sup>	1.8	0.65 mA/cm <sup>2</sup>	3700
coral-like CNTs <sup>61</sup>	4.0		
CNT/TEOS <sup>62</sup>	1.76	0.5 mA/cm <sup>2</sup>	5607
metallic nanowire–graphene hybrid nanostructures <sup>63</sup>	7	300 $\mu\text{A}/\text{cm}^2$	3533
DNW films <sup>Present study</sup>	4.35	3.42 mA/cm <sup>2</sup>	1024

figure captions

#### 4. CONCLUSION

Conducting DNWs films with a carrier concentration of  $\sim 1.0 \times 10^{20} \text{ cm}^{-3}$  and a conductivity of  $186 \text{ S cm}^{-1}$  have been synthesized by using  $\text{N}_2/\text{CH}_4$  plasma. TEM and FESEM analyses portray the feature of nanowire morphology with a length of few hundred nanometers. The SAED pattern and visible-Raman spectrum indicate the coexistence of diamond and graphitic phases that is verified again in the NEXAFS spectrum. The XPS spectrum confirmed the introduction of nitrogen into the DNWs films. Further, the HRTEM image exposes randomly oriented diamond grains on DNWs and graphitic layer encasing the surface of DNWs. STM and STS measurements show up the insulating manner in the interval space between DNWs. It also reveals the highly conducting paths through the graphitic grain boundaries rather than the diamond grains on surfaces of DNWs. Grain boundaries establish conducting channels covering on the whole surface of the DNW and DNWs are electrically contacted to form 3D conducting channels. On the other hand, DNWs films, placed in the 200 nm wide gap between pairing electrodes, were employed for disclosing electron transport at nanometer scale. The temperature dependence of conductivities convinces a

transport mechanism of the Mott's 3D VRH model in DNWs at temperatures ranging from 300 to 20 K. This result points to the hopping demeanor of electron transport between grain boundaries and DNWs. More interestingly, the character of conducting grain boundaries on DNWs can be used to demonstrate an excellent EFE property that evidence high potential applications in field emission or plasma devices.

## AUTHOR INFORMATION

### Corresponding Author

\*E-mail: nhtai@mx.nthu.edu.tw (N.H.T); inanlin@mail.tku.edu.tw (I.N.L.).

### Author Contributions

The manuscript was written through contributions of all authors. All authors have given approval to the final version of the manuscript.

### Notes

The authors declare no competing financial interest.

## ACKNOWLEDGMENTS

This work was supported by the Taiwan National Science Council under Grants NSC 101-2112-M-032 -002-MY2 and NSC 101-2221-E-007-064-MY3.

## REFERENCES

- (1) Zhu, W.; Kochanski, G. P.; Jin, S.; Seibles, L. *J. Appl. Phys.* **1995**, *78*, 2707.
- (2) de Heer, W. A.; Chatelain, A.; Ugarte, D. *Science* **1995**, *270*, 1179.
- (3) Amaratunga, G. A. J.; Silva, S. R. P. *Appl. Phys. Lett.* **1996**, *68*, 2529.
- (4) Sun, M.; Gao, Y.; Zhi, C.; Bando, Y.; Golberg, D. *Nanotechnology* **2011**, *22*, 145705.
- (5) Yamaguchi, H.; Masuzawa, T.; Nozue, S.; Kudo, Y.; Saito, I.; Koe, J.; Kudo, M.; Yamada, T.; Takakuwa, Y.; Okano, K. *Phys. Rev. B* **2009**, *80*, 165321.
- (6) Geis, M. W.; Efreimow, N. N.; Krohn, K. E.; Twichell, J. C.; Lszczarz, T. M.; Kalish, R.; Greer, J. A.; Tabat, M. D. *Nature* **1998**, *393*, 431.
- (7) Okano, K.; Koizumi, S.; Silva, S. R. P.; Amaratunga, G. A. J. *Nature* **1996**, *381*, 140.
- (8) Watanabe, H.; Nebel, C. E.; Shikata, S. *Science* **2009**, *324*, 1425.
- (9) Cui, Y.; Wei, Q.; Park, H.; Lieber, C. M. *Science* **2001**, *293*, 1289–1292.
- (10) Huang, M. H.; Mao, S.; Feick, H.; Yan, H.; Wu, Y.; Kind, H.; Webber, E.; Russo, R.; Yang, Y. *Science* **2001**, *292*, 1897–1899.
- (11) Huang, Y.; Duan, X.; Wei, Q.; Lieber, C. M. *Science* **2001**, *291*, 630–633.
- (12) Rao, S. G.; Huang, L.; Setyawan, W.; Huang, S. *Nature* **2003**, *425*, 36–37.
- (13) Baughman, R. H.; Zakhidov, A. A.; Heer, W. A. de. *Science* **2002**, *297*, 787–792.
- (14) Iijima, S. *Nature* **1998**, *354*, 56–58.
- (15) Ma, D. D. D.; Lee, C. S.; Au, F. C. K.; Tong, S. Y.; Lee, S. T. *Science* **2003**, *299*, 1874–1877.
- (16) Barnard, A. S.; Russo, S. P.; Snook, I. K. *Nano Lett.* **2003**, *3*, 1323–1328.
- (17) Barnard, A. S.; Snook, I. K. *J. Chem. Phys.* **2004**, *120*, 3817–3821.
- (18) Wang, C. X.; Yang, G. W. *Mater. Sci. Eng., R* **2005**, *49*, 157–202.
- (19) Fonoberov, V. A.; Balandin, A. A. *Nano Lett.* **2006**, *6*, 2442–2446.
- (20) Ghosh, S.; Calizo, I.; Teweldebrhan, D.; Pokatilov, E. P.; Nika, D. L.; Balandin, A. A.; Bao, W.; Miao, F.; Lau, C. N. *Appl. Phys. Lett.* **2008**, *92*, 151911.
- (21) Shiomi, H. *Jpn. J. Appl. Phys.* **1997**, *36*, 7745–7748.
- (22) Masuda, H.; Watanabe, M.; Yasui, K.; Tryk, D.; Rao, T.; Fujishima, A. *Adv. Mater.* **2000**, *12*, 444–447.
- (23) Arenal, R.; Bruno, P.; Miller, D. J.; Bleuel, M.; Lal, J.; Gruen, D. M. *Phys. Rev. B* **2007**, *75*, 195431.
- (24) Arenal, R.; Montagnac, G.; Bruno, P.; Gruen, D. M. *Phys. Rev. B* **2007**, *76*, 245316.
- (25) Gruen, D. M. *Annu. Rev. Mater. Sci.* **1999**, *29*, 211–259.
- (26) Sankaran, K. J.; Panda, K.; Sundaravel, B.; Chen, H. C.; Lin, I. N.; Lee, C. Y.; Tai, N. H. *ACS Appl. Mater. Interfaces* **2012**, *4*, 4169–4176.
- (27) Bhattacharyya, S.; Auciello, O.; Birrell, J.; Carlisle, J. A.; Curtiss, L. A.; Goyette, A. N.; Gruen, D. M.; Krauss, A. R.; Schlueter, J.; Sumant, A.; Zapol, P. *Appl. Phys. Lett.* **2001**, *79*, 1441–1443.
- (28) Birrell, J.; Gerbi, J. E.; Auciello, O.; Gibson, J. M.; Gruen, D. M.; Carlisle, J. A. *J. Appl. Phys.* **2003**, *93*, 5606–5612.
- (29) Vlasov, I. I.; Lebedev, O. I.; Ralchenko, V. G.; Goovaerts, E.; Bertoni, G.; Tendeloo, G. V.; Konov, V. I. *Adv. Mater.* **2007**, *19*, 4058–4062.
- (30) Chen, Y. C.; Tai, N. H.; Lin, I. N. *Diamond Relat. Mater.* **2008**, *17*, 457–461.
- (31) Shang, N.; Papakonstantinou, P.; Wang, P.; Zakharov, A.; Palnitkar, U.; Lin, I. N.; Chu, M.; Stamboulis, A. *ACS Nano* **2009**, *3*, 1032–1038.
- (32) Bhattacharyya, S. *Phys. Rev. B* **2004**, *70*, 125412.
- (33) Beloborodov, I. S.; Zapol, P.; Gruen, D. M.; Curtiss, L. A. *Phys. Rev. B* **2006**, *74*, 235434.
- (34) Shah, K. V.; Churochkin, D.; Chiguvare, Z.; Bhattacharyya, S. *Phys. Rev. B* **2010**, *82*, 184206.
- (35) Mareš, J. J.; Hubík, P.; Křištofik, J.; Kindl, D.; Fanta, M.; Nesládek, M.; Williams, O.; Gruen, D. M. *Appl. Phys. Lett.* **2006**, *88*, 092107.
- (36) Bhattacharyya, S. *Phys. Rev. B* **2008**, *77*, 233407.
- (37) Choy, T. C.; Somoza, A. M.; Ortuno, M.; Somoza, A. M. *Appl. Phys. Lett.* **2008**, *92*, 012120.
- (38) Achatz, P.; Williams, O. A.; Bruno, P.; Gruen, D. M.; Garrido, J. A.; Stutzmann, M. *Phys. Rev. B* **2006**, *74*, 155429.
- (39) Gerbi, J. E.; Auciello, O.; Birrell, J.; Gruen, D. M.; Alphenaar, B. W.; Carlisle, J. A. *Appl. Phys. Lett.* **2003**, *83*, 2001–2003.
- (40) Fowler, R. H.; Nordheim, L. *Proc. R. Soc. London, Ser. A* **1928**, *119*, 173–181.
- (41) Thomsen, C.; Reich, S. *Phys. Rev. Lett.* **2000**, *85*, 5214.
- (42) Ferrari, A. C.; Robertson, J. *Phys. Rev. B* **2001**, *63*, 121405.
- (43) Kuzmany, H.; Pfeiffer, R.; Salk, N.; Günther, B. *Carbon* **2004**, *42*, 911–917.
- (44) Vlasov, I. I.; Ralchenko, V. G.; Goovaerts, E.; Saveliev, A. V.; Kanzyuba, M. V. *Phys. Status Solidi (a)* **2006**, *203*, 3028–3035.
- (45) Chang, Y. K.; Hsieh, H. H.; Pong, W. F.; Tsai, M. H.; Chien, F. Z.; Tseng, P. K.; Chen, L. C.; Wang, T. Y.; Chen, K. H.; Bhusari, J. R.; Yang, J. R.; Lin, S. T. *Phys. Rev. Lett.* **1999**, *82*, 5377–5380.
- (46) Joseph, P. T.; Tai, N. H.; Chen, C. H.; Niu, H.; Cheng, H. F.; Pong, W. F.; Lin, I. N. *J. Phys. D: Appl. Phys.* **2009**, *42*, 105403.
- (47) Chen, Y. F. *Surf. Sci.* **1997**, *380*, 199–209.
- (48) Sankaran, K. J.; Kurian, J.; Chen, H. C.; Dong, C. L.; Lee, C. Y.; Tai, N. H.; Lin, I. N. *J. Phys. D: Appl. Phys.* **2012**, *45*, 365303.
- (49) Teii, K.; Ikeda, T. *Diamond Relat. Mater.* **2007**, *16*, 753–756.
- (50) Mott, N. F. *Conduction in Non-crystalline Materials*; Clarendon Press: Oxford, U.K., 1993; p 32.
- (51) Liu, J.; Zhirnov, V. V.; Myers, A. F.; Wojak, G. J.; Choi, W. B.; Hren, J. J.; Wolter, S. D.; McClure, M. T.; Stoner, B. R.; Glass, J. T. *J. Vac. Sci. Technol. B* **1995**, *13* (2), 422–426.
- (52) Zhu, W.; Kochanski, G. P.; Jin, S. *Science* **1998**, *282*, 1471–1473.
- (53) Tarntair, F. G.; Chen, L. C.; Wei, S. L.; Hong, W. K.; Chen, K. H.; Cheng, H. C. *J. Vac. Sci. Technol. B* **2000**, *18*, 1207–1211.
- (54) Pradhan, D.; Lin, I. N. *ACS Appl. Mater. Interfaces* **2009**, *1*, 1444–1450.
- (55) Thomas, J. P.; Chen, H. C.; Tai, N. H.; Lin, I. N. *ACS Appl. Mater. Interfaces* **2011**, *3*, 4007–4013.

(56) Thomas, J. P.; Chen, H. C.; Tseng, S. H.; Wu, H. C.; Lee, C. Y.; Cheng, H. F.; Tai, N. H.; Lin, I. N. *ACS Appl. Mater. Interfaces* **2012**, *4* (10), 5103–5108.

(57) Sankaran, K. J.; Kunuku, S.; Lou, S. C.; Kurian, J.; Chen, H. C.; Lee, C. Y.; Tai, N. H.; Leou, K. C.; Chen, C.; Lin, I. N. *Nanoscale Res. Lett.* **2012**, *7*, 522.

(58) Varshney, D.; Rao, C. V.; Guinel, M. J. F.; Ishikawa, Y.; Weiner, B. R.; Morell, G. *J. Appl. Phys.* **2011**, *110*, 044324.

(59) Nguyen, D. D.; Tai, N. H.; Chen, S. Y.; Chueh, Y. L. *Nanoscale* **2012**, *4*, 632–638.

(60) Shang, N. G.; Papakonstantinou, P.; McLaughlin, J.; Chen, W. C.; Chen, L. C.; Chu, M.; Stamboulis, A. *J. Appl. Phys.* **2008**, *103*, 124308.

(61) Shang, N. G.; Li, C. P.; Wong, W. K.; Lee, C. S.; Bello, I.; Lee, S. T. *Appl. Phys. Lett.* **2003**, *81*, 5024–5026.

(62) Jeong, H. J.; Jeong, H. D.; Kim, H. Y.; Kim, J. S.; Jeong, S. Y.; Han, J. T.; Bang, D. S.; Lee, G. W. *Adv. Funct. Mater.* **2011**, *21*, 1526–1532.

(63) Arif, M.; Heo, K.; Lee, Yang, B.; Lee, J.; Seo, D. H.; Seo, S.; Jian, J.; Hong, S. *Nanotechnology* **2011**, *22*, 355709.

(64) Wang, Q. H.; Setlur, A. A.; Lauerhaas, J. M.; Dai, J. Y.; Seeling, E. W.; Chang, R. P. H. *Appl. Phys. Lett.* **1998**, *72*, 2912–2913.